Supplementary Information for

Massive Acceleration of S_N2 Reaction Using the Oriented External Electric Field

Chun Tang,[a,1] Meiling Su,[a,1] Taige Lu,[a,1] Jueting Zheng,[a,1] Juejun Wang,[a] Yu Zhou,[a] Yu-Ling Zou,[a] Wenqing Liu,[a] Ruiyun Huang,[a] Wei Xu,[a] Lijue Chen,[a] Yanxi Zhang,[a] Jie Bai,[a] Yang Yang,[a] Jia Shi,[a] Junyang Liu,[a,*] Wenjing Hong[a]

[a]State Key Laboratory of Physical Chemistry of Solid Surfaces, College of Chemistry and Chemical Engineering, Xiamen University; Xiamen 361005.

[1]C. Tang, M. Su, T. Lu and J. Zheng contributed equally to this work.

*Corresponding Author(s): jyliu@xmu.edu.cn

Supplementary Text

1. Materials

Trichlorobenzene (TCB) was purchased from Sigma-Aldrich. 1-Iodooctane (**IOA**) was purchased from Aladdin. All chemicals, reagents, and solvents from commercial sources were used as received without further purification. ^{1}H NMR spectra were recorded with a Bruker AVANCE NEO 500 (500MHz). The spectra were referenced to residual proton-solvent references.

2. Molecular synthesis

4-(4-(methylthio)phenyl)pyridine (**MPP**)

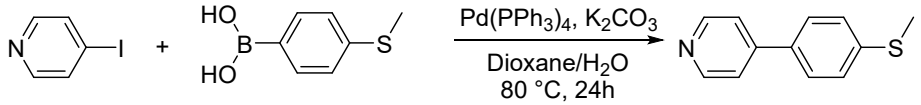

The synthesis of 4-(4-(methylthio)phenyl)pyridine (**MPP**) was according to the previous literature[1]. 4-Iodopyridine (816.0 mg, 4.0 mmol), (4-(methylthio) phenyl) boronic acid (840.5 mg, 5.0 mmol), $Pd(PPh_3)_4$ (231.2 mg, 5 mol%) and K_2CO_3 (1.4 g, 10 mmol) were dissolved in a mixture of dioxane (15 mL) and deionized water (1 mL). The suspended solution was then degassed and refluxed under the protection of N_2 for 24 h. The reaction mixture was then cooled to room temperature and treated with water, followed by the extraction using CH_2Cl_2. Then the products were further purified by column chromatography on silica gel (DCM/Et_3N = 10/1) to give the final product as a white solid (650.0 mg, yield 80 %). ^{1}H NMR (500 MHz, $CDCl_3$): δ 8.68 (d, 2H), 7.60 (d, 2H), 7.52 (d, 2H), 7.38 (d, 2H), 2.55 (s, 3H).

4-(4-(methylthio)phenyl)-1-octylpyridin-1-ium iodide (**OMPP**)

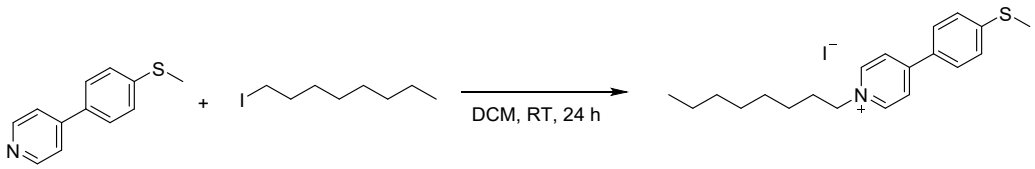

The synthesis of 4-(4-(methylthio)phenyl)-1-octylpyridin-1-ium iodide (**OMPP**) was according to the previous literature[1]. 4-(4-(Methylthio)phenyl)pyridine (**MPP**) (603.0 mg, 3.0 mmol) and 1-iodooctane (864.2 mg, 3.6 mmol) were dissolved in DCM (20 mL). The suspended solution was then degassed and stirred under the protection of N_2 for 24 h. The target product was precipitated from the reaction mixture under reduced pressure distillation as a pale-yellow solid (1011.3 mg, yield 77.4 %). ^{1}H NMR (500 MHz, $CDCl_3$): δ 9.15 (d, 2H), 8.24 (d, 2H),7.78 (d, 2H),7.43 (d, 2H), 4.82 (t, 2H), 2.59 (s, 3H),1.47 (m, 8H), 0.90 (d, 3H).

4-(4-(Methylthio)phenyl)-1-methylpyridin-1-ium iodide (**MMPP**)

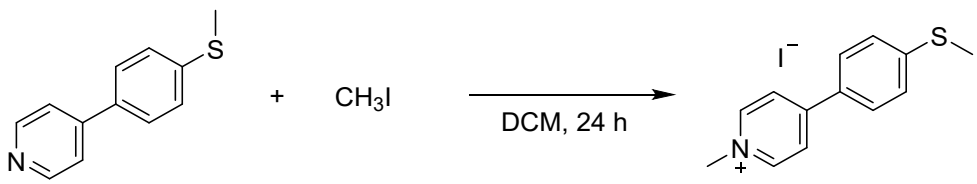

The synthesis of 4-(4-(methylthio)phenyl)-1-octylpyridin-1-ium iodide (**MMPP**) was similar to **OMPP**. 4-(4-(methylthio)phenyl)pyridine (**MPP**) (603.0 mg, 3.0 mmol) and iodomethane (413.6 mg, 3.6 mmol) were dissolved in DCM (20 mL). The suspended solution was then degassed and stirred under the protection of N_2 for 24 h. The target product was precipitated from the reaction mixture under reduced pressure distillation as a pale-yellow solid (1001.3 mg, yield 98.5 %).

3. The STM-BJ measurements

Preparation for the experiments: Gold wire (99.99%, 0.25 mm diameter) is purchased from Beijing Jiaming Platinum Nonferrous Metal Co, Ltd. for the fabrication of the STM tip. The gold tip is cleaned by butane flame to form a gold bead. Substrates are prepared by depositing a 100 nm thick gold film on a silicon wafer. The gold-coated substrate is cleaned by immersing in piranha solution ($V(H_2SO_4):V(H_2O_2)$ = 3:1 CAUTION! piranha solution is highly corrosive) for about 4 hours and is rinsed with fresh deionized water for 5 minutes. After this time, the substrate is moved into fresh deionized water, and the boiling procedure repeats for a total of three cycles. Then, the substrate can be used after drying.

The sample preparation: The target molecules of **MPP** and **IOA** were mixed with TCB into a solution with a concentration of 1 mM and 100 mM. To prevent leakage of solvent and contamination by other impurities, we sealed the solution of the reaction system in a polytef liquid cell containing a plastic O-ring (perfluoroelastomer 5.0*1.0, ZOE Sealing Technology Development Co. Ltd.). Before the experiments, Piranha solution followed by 18.2 MΩ cm^{-1} Milli-Q water (Millipore) was used to clean the ploytef cells and gold substrates.

Blank experiment: All the single-molecule conductance measurements were carried out with a homemade STM-BJ device at room temperature in a solution containing 15 mL 1 mM of the target molecule in TCB. In order to calibrate the stretching rate of gold electrodes, before adding the **MPP** solution, we used the pure TCB solvent without the target molecule as a blank experiment for the calibration of distance for STM-BJ experiments.

4. Flicker noise analysis

We analyzed the noise of conductance traces and plotted the noise histogram to distinguish two ways of charge transport by the flicker noise analysis method as previously reported by Latha *et al.*[2]. A two-dimensional flicker noise density histogram is used to analyze suspended traces. We suspend the retracting process of the tip for 150 ms to collect suspended traces. Then, we integrate the noise power from 10^2 - 10^3 Hz signals by fast Fourier transform. The noise power is normalized by the average conductance of each sampling. All noise points are further analyzed by two-dimensional Gaussian fitting to distinguish two different flicker noise signals well. In order to evaluate the transport of molecules, we test a series of values n from 1 to 2 as the step of 0.1. The noise power scales with an exponent of conductance G_0^n, and the n

is determined when we get the minimum of the correlation between noise power and conductance.

5. Combined Raman measurement

In situ SERS measurements offered a complementary approach in addition to single-molecule electrical characterization to verify our hypothesis of species in molecular junctions. A previous fabrication method of microchips for MCBJ normally used polyimide as the insulating and sacrificial layer to suspend the gold nanobridges. However, to avoid unnecessary Raman signal interference from the polyimide layer, we developed a new method to replace the polyimide with silicon oxide. Besides, to simplify the fabrication process, we introduced focus ion beam milling (Zeiss Orion Nanofab) to pattern the gold electrode with linewidth in micrometer scale by photolithography and lift-off processes into a nanobowtie directly[3]. After a combined dry and wet etching of the silicon oxide layer, a gold nanobridge was successfully fabricated, with ~70 nm in width and 50 nm in thickness, respectively (Fig. S27a). The nanobridge was further stretched into nanoelectrodes paired with nanogap during the MCBJ experiment (see SEM image in the inset of Fig. S27a). Afterward, the MCBJ chip was assembled onto a homebuilt MCBJ setup under a modified confocal Raman spectroscopic instrument for further measurements. As shown in Fig. 3B, the difference in signal-to-noise ratio between the NPs-SERS and STM-BJ Raman is reasonable, since the STM-BJ Raman can only detect the signal of very few components between the two electrodes, while the NPs-SERS (see Fig. S27b) can detect three more orders of magnitude molecules than STM-BJ Raman.

6. Theoretical calculation

The molecule structures of **MPP** and **OMPP** were calculated with the optimized structure using B3LYP functional combined with 6311++g** basis set for all the atomic elements contained in the molecules. Molecular structures were optimized without any symmetry constraint. The optimized molecular structures were then placed between two gold electrodes to construct the single-molecule devices in the QuantumATK Q-2019.12 package. As shown in Fig. S31B, because of the uncertainty of the gold electrodes contact configuration or solution environment, the Fermi level in experiments is not always consistent with the calculations. Although **OMPP** shows a slightly higher transmission coefficient than **MPP** at the Fermi level, **MPP** shows an even higher transmission than **OMPP** in a wide range between the energy of HOMO and LUMO, which is consistent with the conductance trend in the experiment.

7. Automated data selection algorithm

We adopt a region-based automated data selection algorithm[4] to determine whether a single-molecule junction was detected for every conductance trace we recorded during the reaction measured by STM-BJ.

We first counted data points for each conductance-displace trace within the region where the molecule was formed. The region R_{mol} is identified as the conductance interval for a certain molecule. If the number of data points in region R_{mol} is fewer than the average number of data points, T, it was regarded as the absence of a molecular junction, and that conductance trace could not be counted because it belongs to the class of direct tunnelling. If the trace has more data points than T in region R_{mol}, it would be recognized that a trace witnessed the formation of one molecular junction.

The algorithm to find data points T signifying the formation of the molecular junction works as following steps:

Step 1: Thousands of conductance-distance traces during the reaction were sampled from conductance G_{min} to G_{max} with the same sampling rate and same bin size dividing the conductance axis. Then 1D conductance histograms of all traces were constructed. Here a histogram function H(x) was defined, where x represents the conductance variable of the statistical bins.

Step 2: The conductance region, R_{mol}, was set based on the molecular conductance distribution:

$$R_{mol} = \{G|10^{-2} \leq G \leq 10^{-4}\}$$

The reason for choosing this region is that in the 1D conductance histogram, the peak accounting for molecular junctions can be fully covered (Fig. 1c).

Step 3: Count the number of the data points (T) in the region R_{mol}:

$$T = \frac{S_{R_{mol}}}{S}$$

Where T represents the average number of data points in the conductance region R_{mol}, it can be used as a threshold to judge whether there is a plateau in region R_{mol}. $S_{R_{mol}}$ and S are the areas of the 1D histogram in the region R_{mol} and the whole region. The calculation process is shown below:

$$S = \int_{G_{min}}^{G_{max}} H(x)dx$$

$$S_{R_{mol}} = \int_{10^{-4}}^{10^{-2}} H(x)dx$$

Step 4: Identify and count traces according to threshold T. The number of data points was counted in the region R_{mol} from the 1D histogram of conductance-distance trace, and if the number $\geq$ T, then it is labeled as a trace with a junction in region R_{mol}.

Step 5: Based on this method, we set a certain time interval (20 minutes, for example) to obtain junction formation possibilities of a certain number of curves. Finally, all possibilities of certain time intervals were plotted to generate the result.

8. Single-molecule junction measurements

Sample preparation: To easily contact the gold electrode, we designed the molecule with pyridyl anchors in para positions, named **MPP**, i.e., 4-[4-(methylthio)phenyl]pyridine. Afterward, 100 mM of **IOA** (1-iodooctane) solution with the same solvent, which is commercially available, was added to the solution of **MPP**. The single-molecule conductance was measured using the STM-BJ technique at room temperature in the TCB with a concentration of 1 mM, and 50 mV bias voltage with a sampling rate of 20 *k*Hz was applied between the two electrodes. Target molecules of **MPP** and **IOA** were mixed with TCB into a solution with a concentration of 1 mM and 100 mM. To prevent leakage of solvent and contamination by other impurities, we sealed the solution of the reaction system in a polytef liquid cell containing a plastic O-ring (perfluoroelastomer 5.0*1.0, ZOE Sealing Technology Development Co. Ltd.). Before the experiments, Piranha solution followed by 18.2 MΩ cm^{-1} Milli-Q water (Millipore) was used to clean the ploytef cells and gold substrates.

Single-molecule conductance monitoring during the reaction: Since the electrical signal monitoring is an *in situ* measuring technique for the single-molecule event, each current jump and drop originated from a single guest molecule binding and detaching to a host. Therefore, this host-guest (de)formation under different biases could be evaluated through the statistical peaks of the corresponding histograms of current drop (jump)s[5]. The STM-BJ involves the formation of the single-molecule junction as recorded by each intercepted conductance-distance trace[6]. Hence, there's an equal possibility for each molecule in the solution grabbed by the electrode pair. As a result, the relative displacement distribution histogram of each species summarized at each time scale could be used to calculate each proportion in the solution[7]. Then the kinetic reaction information can be extracted.

Reaction kinetics under different bias voltages: In order to confirm the electric field activation of the Menshutkin reaction process, parallel *in situ* electrical characterizations under different bias voltages are performed using the same concentration of the reagents in the same TCB solution under the same measuring conditions, setting the bias voltage to 20, 50, 70, 80 and 100 mV, respectively. As the bias voltage increases, the whole reaction accelerates. The k_{20} is fitted to be 1.48×10^{-2} min^{-1}, the k_{50} is fitted to be 2.08×10^{-2} min^{-1}, the k_{70} is fitted to be 5.37×10^{-2} min^{-1}, the k_{80} is fitted to be 5.28×10^{-2} $min^{-1,}$ and the k_{100} is fitted to be 9.60×10^{-2} min^{-1}. The experimental results show that the reaction rate gradually enhances as the bias voltage increases, which further proves the selective activation effect of the electric field during the reaction process.

Reaction kinetics under different tip stretching speeds: We carried out the control experiment by changing the tip speed, which would change the sampling speed. When the tip speed used in the STM-BJ measurements was increased from 24 nm/s (the original value) to 36 nm/s and then to 48 nm/s (twice as the original value), the reaction rate does not show significant change, suggesting that the localized electric field in STM-BJ catalyzes the reaction in the nano-confinement space, rather than capturing the reactant and converting it into products one by one.

Measurement of the mixed solution: To further verify the reliability to use the ratios of peak areas during STM-BJ to determine the component ratio in solution, we conduct the STM-BJ measurement using the solution of the mixed solution containing **MPP** and **OMPP** with a certain ratio (9:1, 4:1, 1:1, 1:4, and 1:9). As shown in Fig. S13, the mixed ratios show a linear dependence to the component ratio, suggesting that **MPP** and **OMPP** exhibit almost identical probability to be captured within the nanogap. Therefore, the relative probability can be used to determine the concentration ratio between **MPP** and **OMPP** in the reaction mixture.

Calculation of snap-back distance: The 1D conductance histogram and 2D conductance-distance histogram in Fig. S11A and B, respectively, show direct tunneling and apparent non-plateau features, which suggests a pure and clean environment inside the gap between the two electrodes. According to the measured tunneling decay constant ($\log(\Delta G/G_0)/\Delta z$ = -5.5 nm^{-1}) in the same solvent using the STM-BJ technique, we calibrated the relative displacement in the conductance range from $10^{-3.5}$ G_0 to 10^{-5} G_0 to be ~0.27 nm (-1.5/-5.5 = ~0.27 nm)[8]. In addition, the snap-back distance is calculated. Since a perfect linear atomic chain of gold has a conductance of G_0, we presume that $\log(G/G_0) = -\Delta z$, where $z = 0$ corresponds to the point at which the distance between the terminating gold atoms is equal to the equilibrium gold-gold separation. As for the measured separation $\Delta z = z - z_{corr}$, where z_{corr} is the snap-back distance, a plot of $\log(G/G_0)$ versus Δz has a slope of $-\alpha$ and an intercept of αz_{corr}.

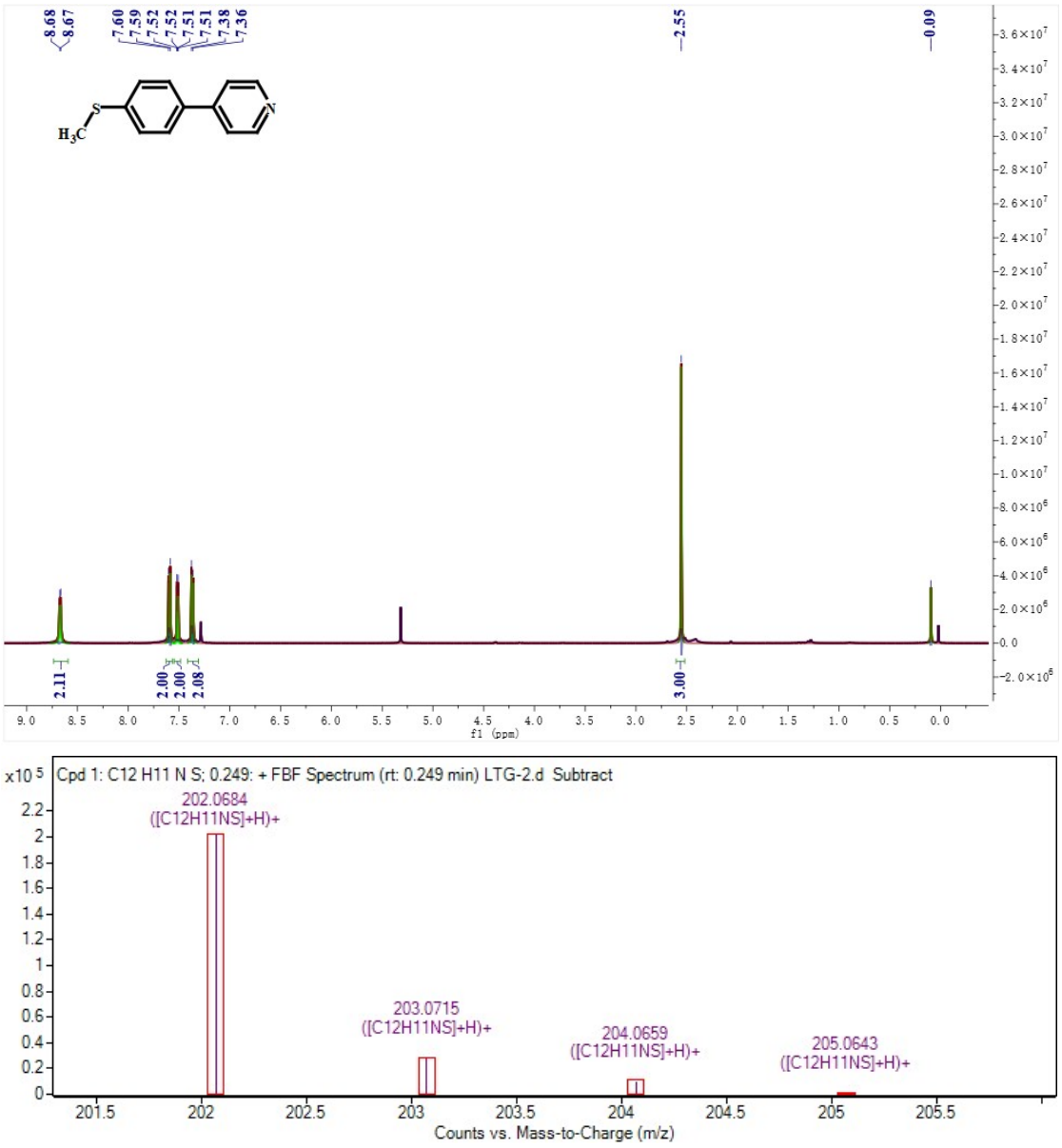

Fig. S1. ^{1}H NMR (500 MHz in $CDCl_3$, top) and HRMS (bottom) spectra of MPP.

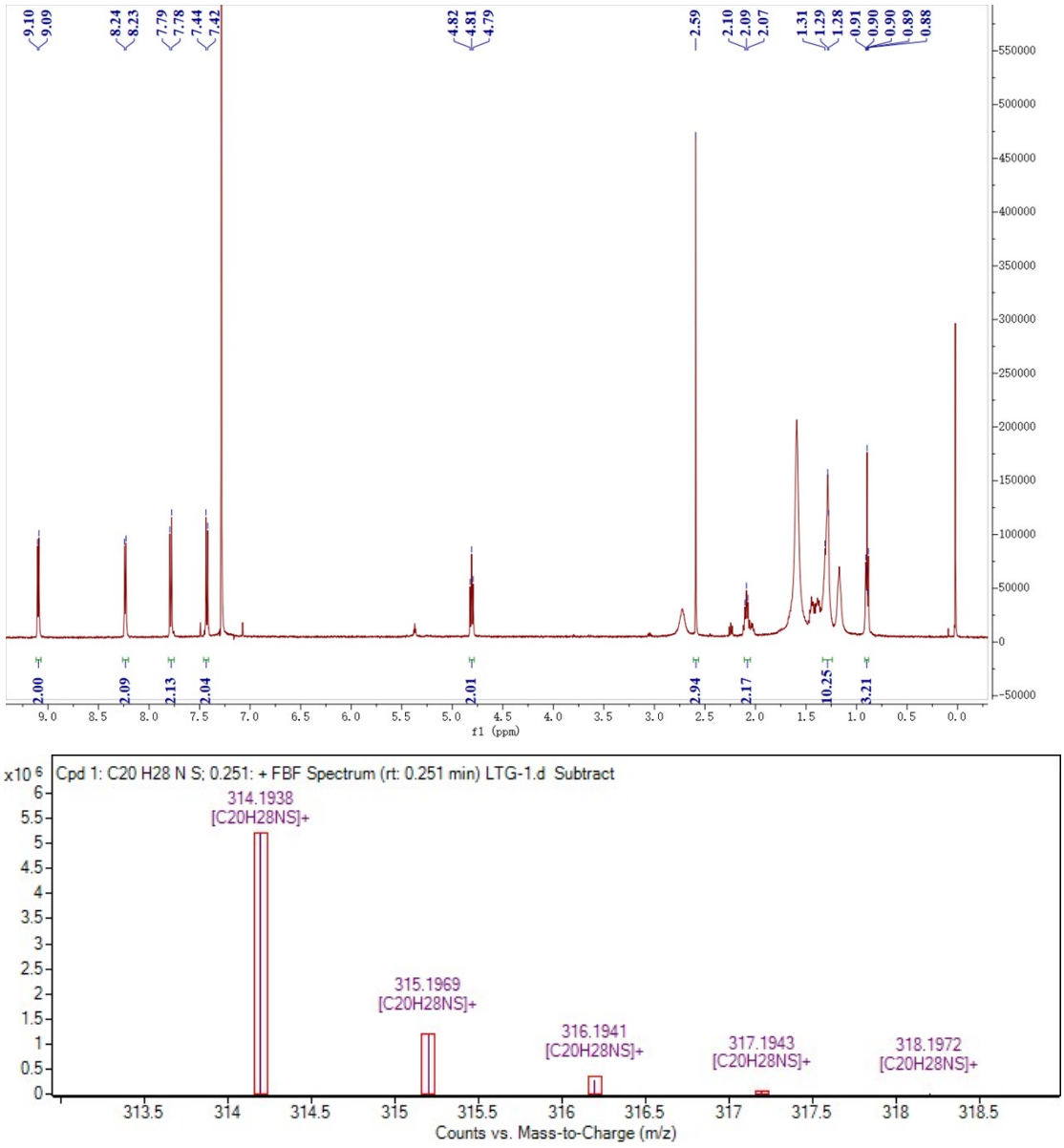

Fig. S2. ^{1}H NMR (500 MHz in $CDCl_3$, top) and HRMS (bottom) spectra of OMPP.

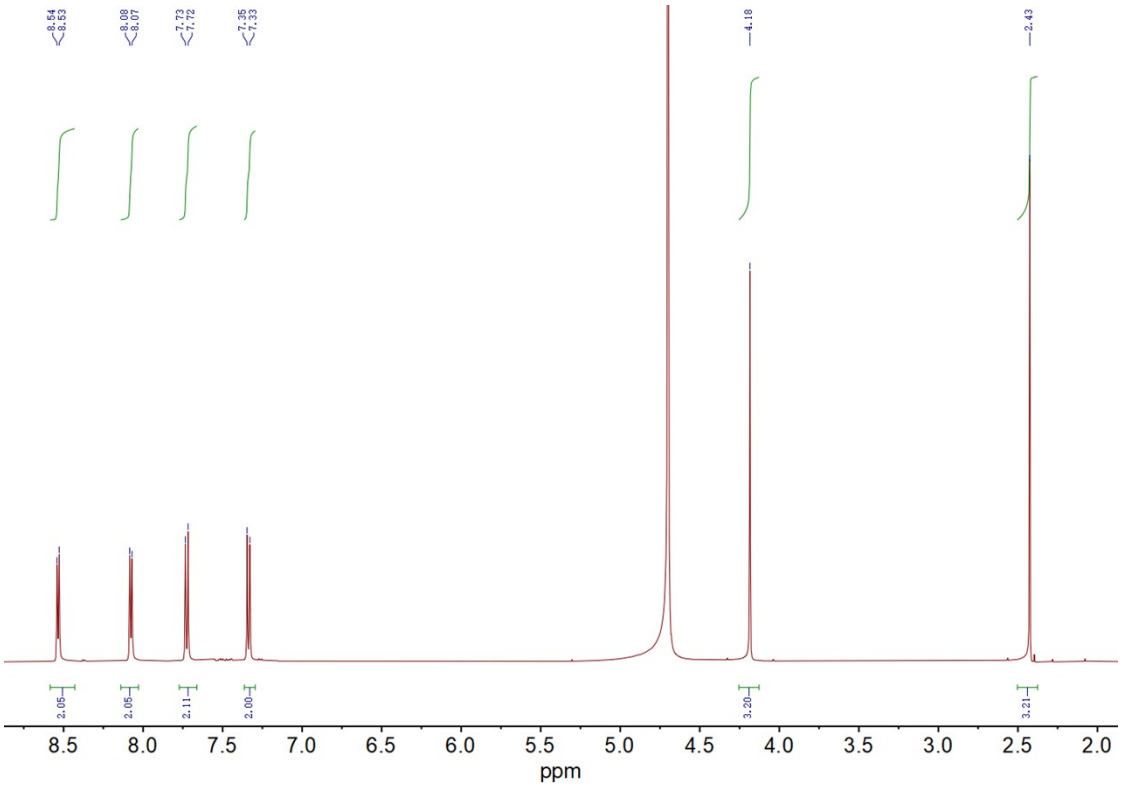

Fig. S3. ^{1}H NMR (500 MHz in D_2O) spectra of MMPP.

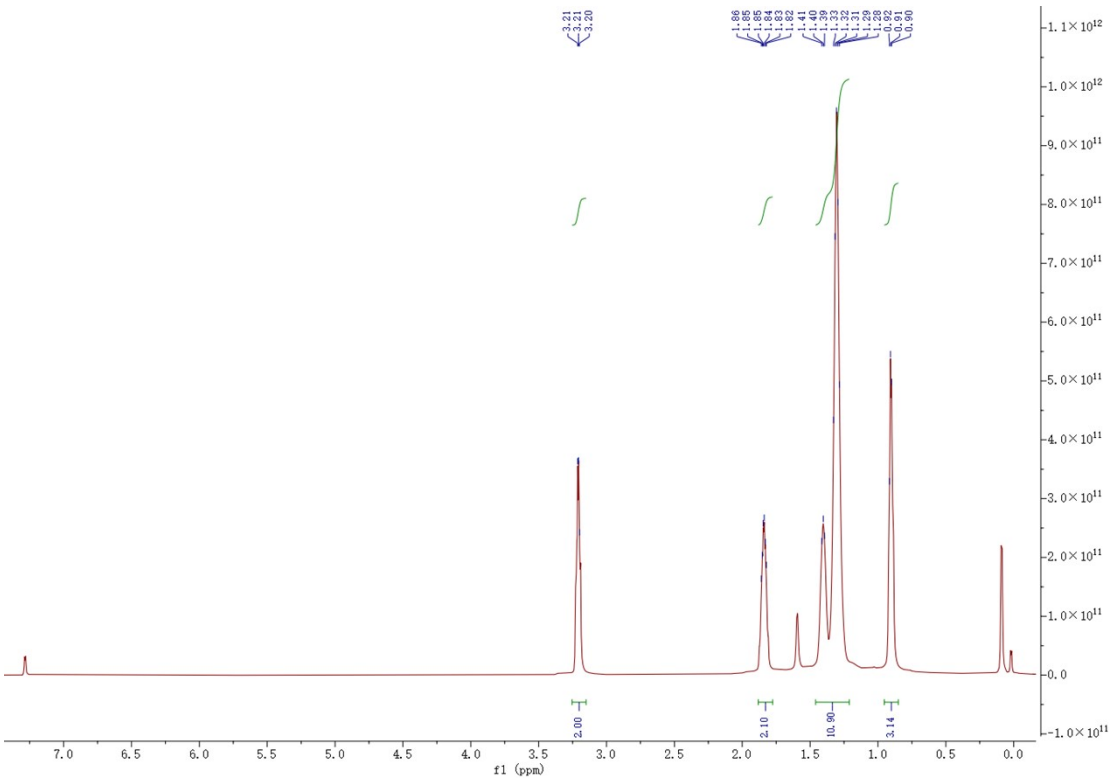

Fig. S4. The characterization spectra of NMR of IOA.

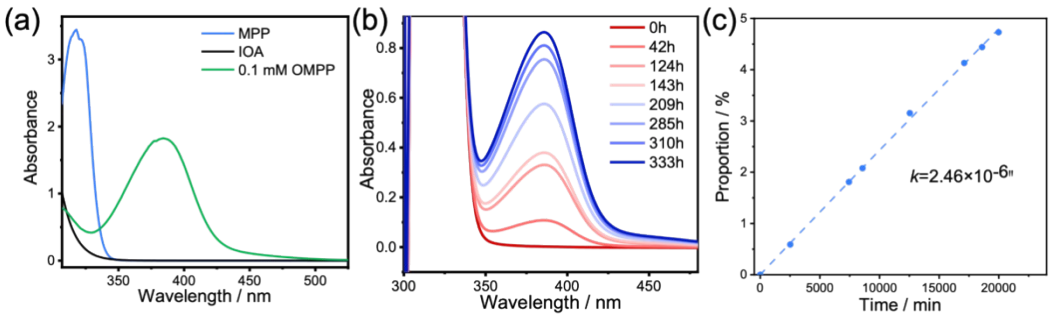

Fig. S5. UV-Vis absorption spectra. (a) **MPP**, **IOA**, and 0.1mM **OMPP** in TCB, respectively. The 0.1 mM **OMPP** solution shows the maximum absorption peak at 384nm. (b) In situ UV-Vis monitoring of the reaction under the same condition in TCB as conductance detection. (c) The fitted proportions of **OMPP** (i.e., conversion rates of the reaction) are extracted from the maximum absorption peak at 384 nm, and the conversion rates extracted from the maximum absorption peak can be obtained as k=2.46×10^{-6} min^{-1}.

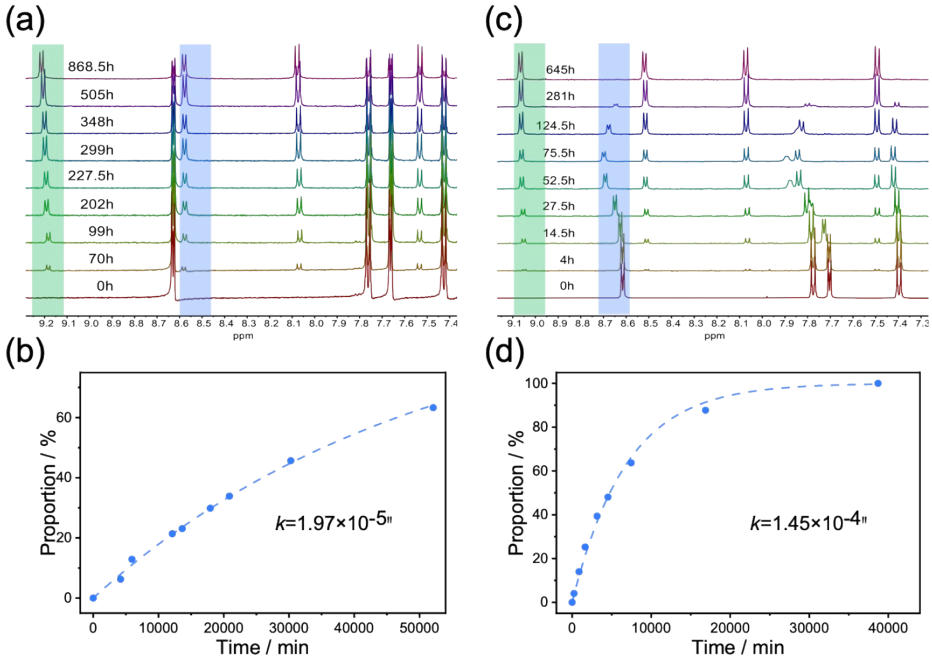

Fig. S6. *In situ* ^{1}H NMR spectra evolution during the whole reaction. *In situ* ^{1}H NMR spectra evolution for the treatment of **MPP** (1 mM) with **IOA** (100 mM) in the acetone (a) and dimethyl sulfoxide (DMSO) (c) solvent in an NMR tube. (b and d) The fitted proportions of **OMPP** (i.e., conversion rates of the reaction) are extracted from NMR integrals. During the reaction process, there only exist two species of compounds **MPP** and **OMPP**, which enable the formation of the molecular junction so that the conversion can be determined by the concentration ratio, which is derived from the integration of ^{1}H NMR. For example, in DMSO solvent, the concentration ratio of **MPP**/**OMPP** is derived from the integration of $H_{\mathbf{MPP}}$ (~8.65) of **MPP** and $H_{\mathbf{OMPP}}$ (~9.05) of **OMPP**. Therefore, the conversion rates can be obtained as 1.97×10^{-5} min^{-1} and 1.45×10^{-4} min^{-1} in acetone and dimethyl sulfoxide, respectively.

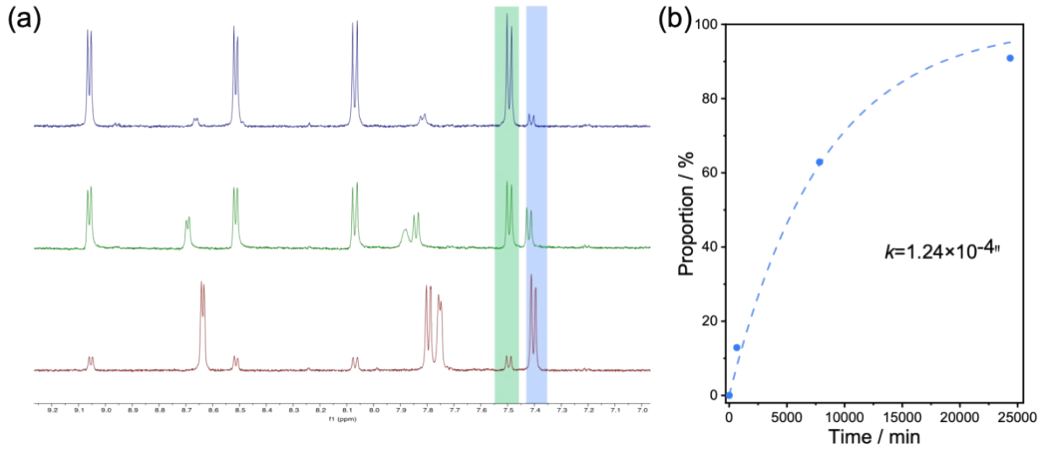

Fig. S7. *In situ* ^{1}H NMR spectra evolution in the solvent of DMSO with a piece of gold wire added. (a) *In situ* ^{1}H NMR spectra evolution for the treatment of **MPP** (1 mM) with **IOA** (100 mM) in DMSO solvent and a piece of gold wire (1 cm) in an NMR tube. (b) The fitted proportion of **OMPP** (i.e., the conversion rate of the reaction) is extracted from NMR integrals: $H_{\mathbf{MPP}}$ (~7.39) of **MPP** and $H_{\mathbf{OMPP}}$ (~7.50) of **OMPP**. The conversion rate can be obtained as k=1.24×10^{-4} min^{-1}. The reaction rate is almost same with the solution without the gold.

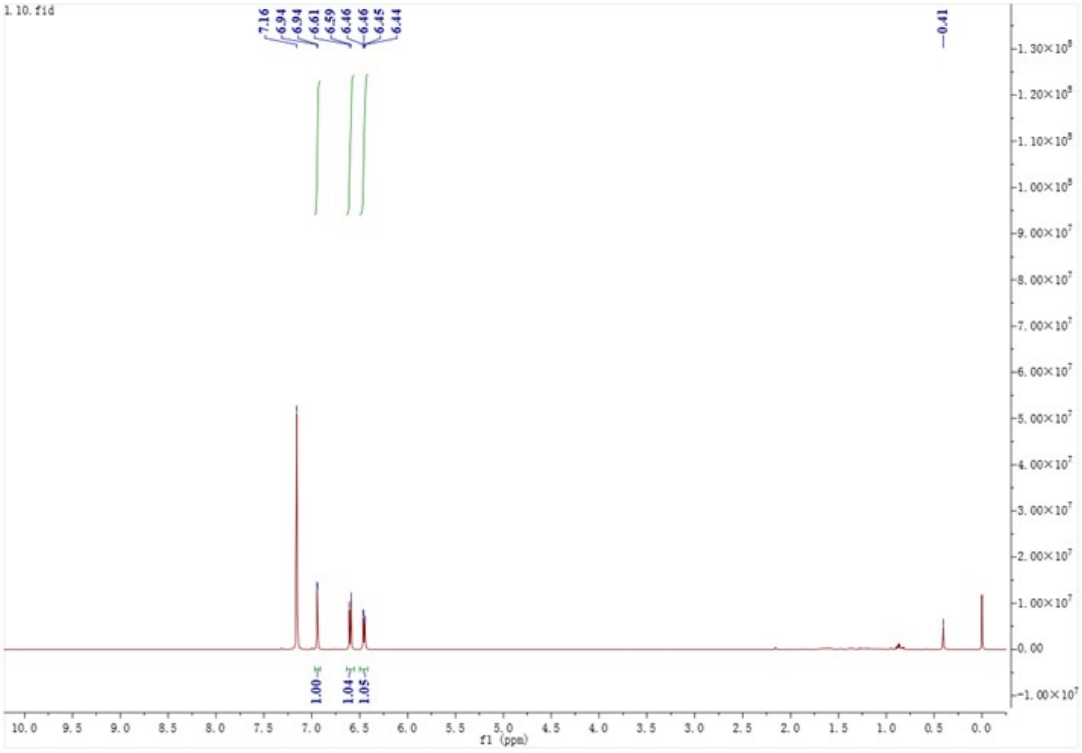

Fig. S8. ^{1}H NMR spectra of TCB (500 MHz in C_6D_6) exposed to white light.

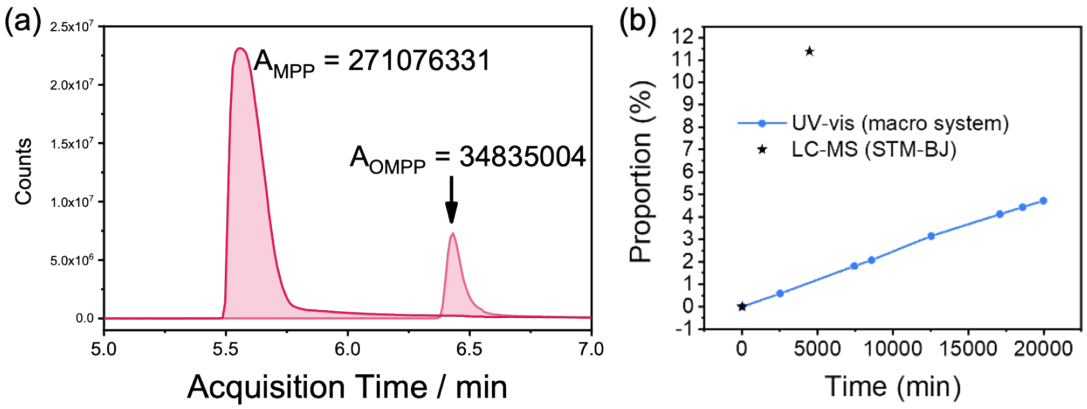

Fig. S9. LC-MS ex-situ characterization after the STM-BJ measurement. (a) LC peaks of the solution in the liquid cell after the 8-hour STM-BJ measurement under a bias of 50 mV. (b) Conversion in the liquid cell by STM-BJ and the quartz cell on the macro scale. Star: STM-BJ; blue line: macro system.

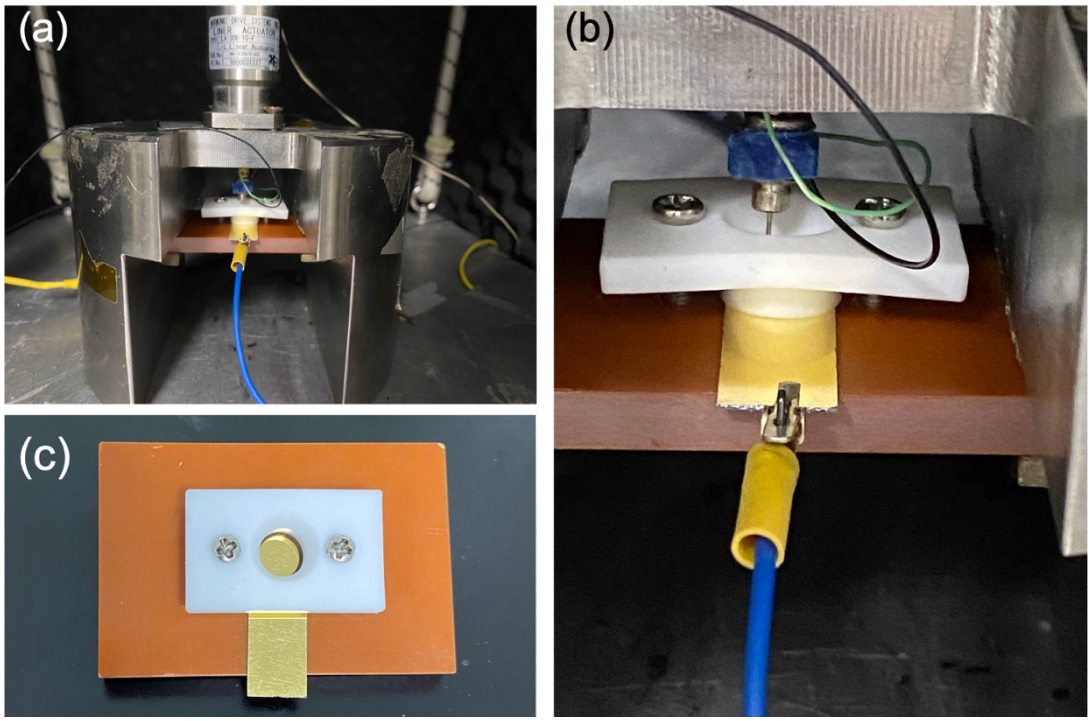

Fig. S10. STM-BJ setup. The STM-BJ setup from (a) the full view and (b) the enlarged view of the substrate with (c) the liquid cell.

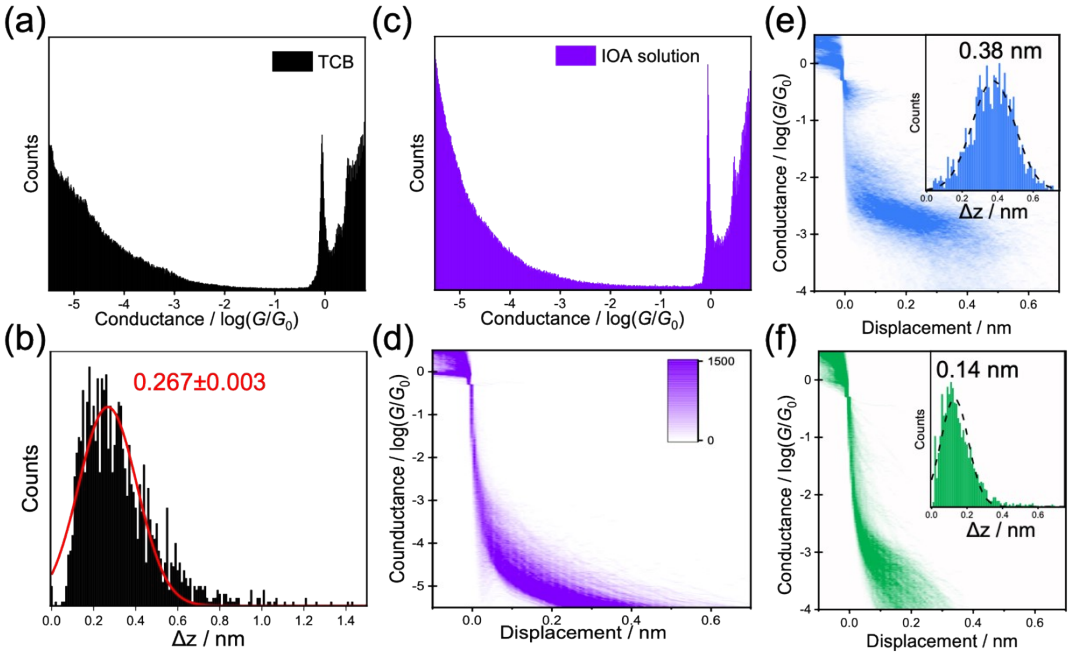

Fig. S11. Single-molecule conductance measurements of solvent, IOA, MPP and OMPP solution. The STM-BJ experiment in pure solvent without adding molecules with (a) 1D conductance histogram for the TCB solvent and (b) the relative displacement distribution histogram determined from the conductance range from $10^{-3.5}$ G_0 to $10^{-5.0}$ G_0. The peak data was obtained by Gaussian function fitting. The clean background suggested that no molecular junction was formed during the experiment with pure solvent. (c) 1D conductance histogram and (d) 2D conductance-distance histogram of 100mM IOA. Each was constructed from 2000 conductance-distance traces. (e) **MPP** and (f) **OMPP** traces and plateau profiles were determined from 2D histograms ranging between $10^{-3.6}$ G_0 and $10^{-0.3}$ G_0. Blue: **MPP**; green: **OMPP**; Insets: plateau distributions of **MPP** and **OMPP**.

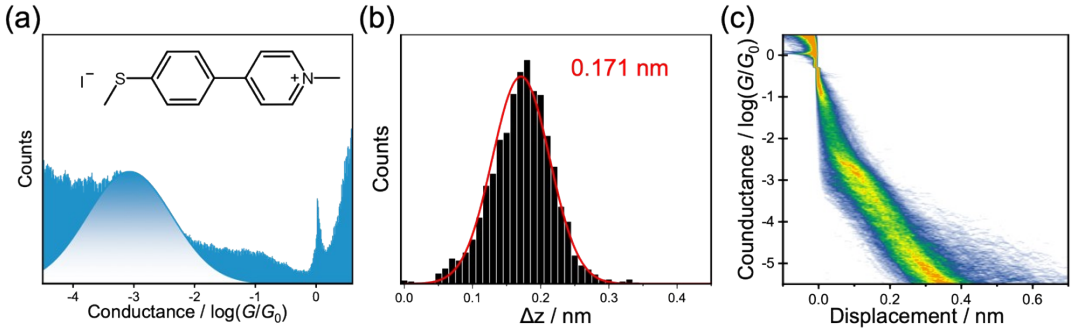

Fig. S12. Single-molecule conductance measurement of MMPP. (a) 1D conductance histogram compiled from 2233 traces; Inset: the structural formula for the MMPP molecule. (b) The relative displacement distribution histogram determined from the conductance range from $10^{-0.3}$ G_0 to $10^{-3.6}$ G_0. (c) 2D conductance-distance histogram.

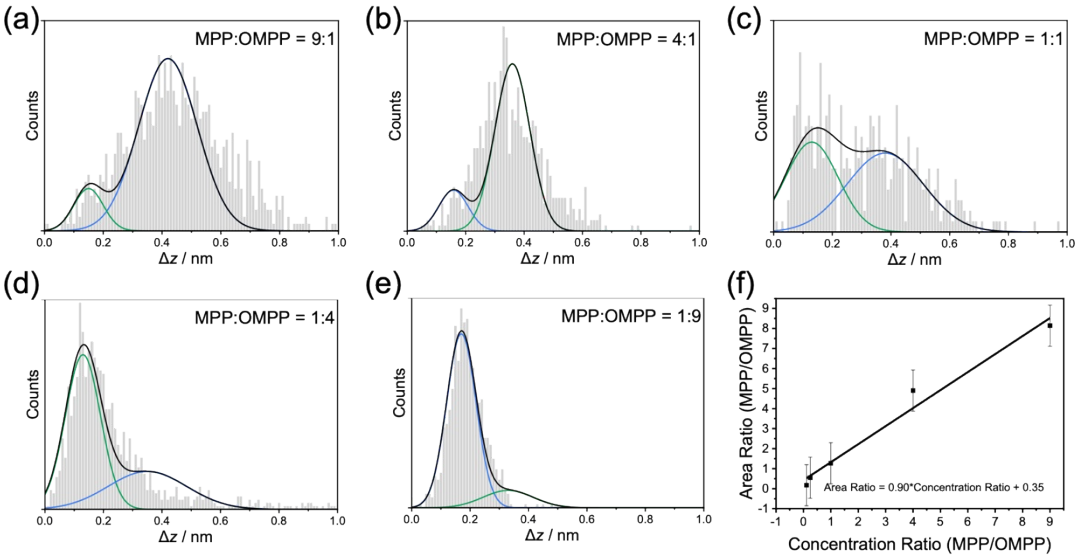

Fig. S13. Single-molecule conductance measurement of the mixed solution. (a-e) Gaussian bimodal fitting of plateau lengths data of the solution containing **MPP** and **OMPP** with a ratio of 9:1, 4:1, 1:1, 1:4 and 1:9, respectively. (f) Linear fitting of the Gaussian bimodal fitting and concentration ratio.

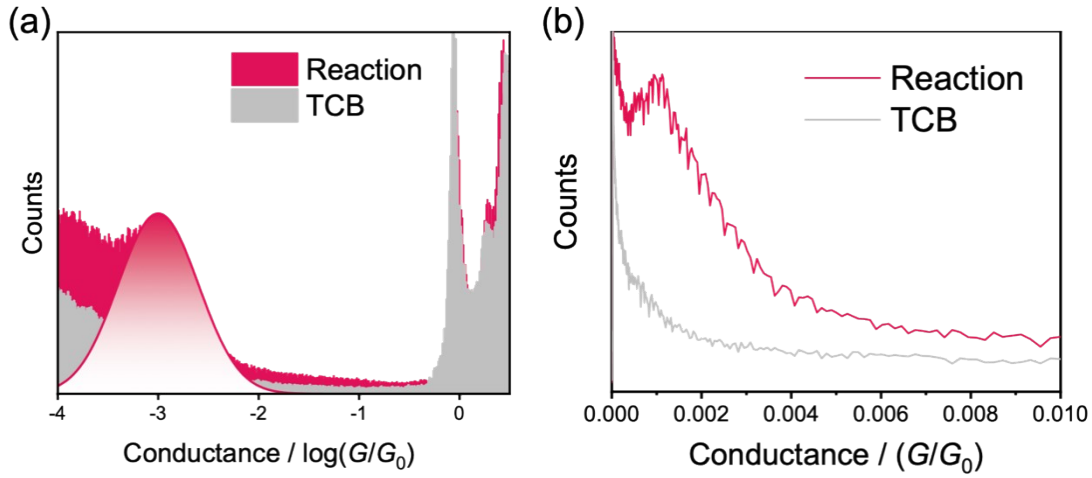

Fig. S14. 1D Histograms of log-binned and linear-binned reaction and TCB. Log-binned (a) and linear-binned (b) 1D histograms of **OMPP** (magenta) and the TCB solvent. The histogram of the reaction shows a molecular peak around 10^{-3} G_0, and the red curve in the log-binned histogram is fitted via Gaussian.

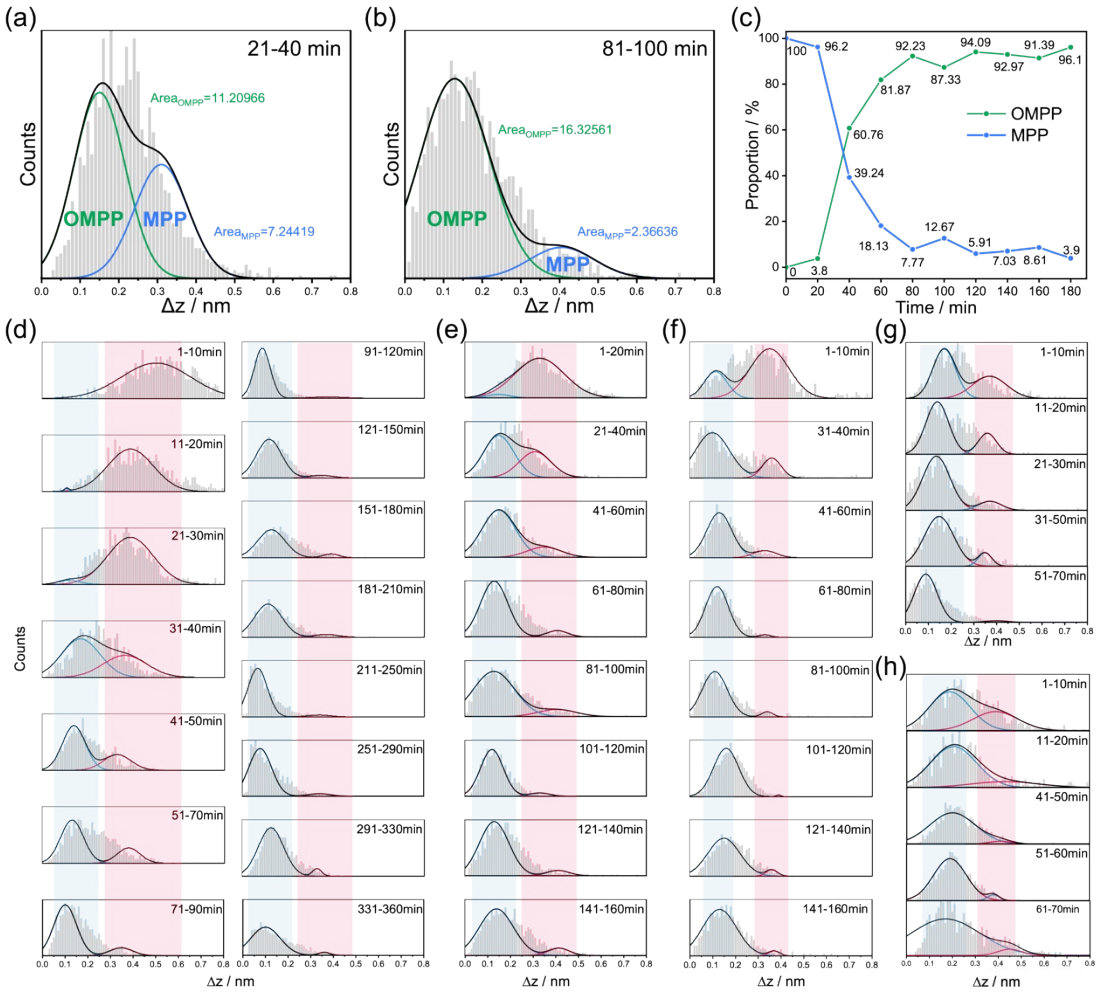

Fig. S15. Reaction kinetics of single-molecule junctions under different bias voltages. (a and b) Determination of the percentages of **MPP** and **OMPP** from plateau histograms. Histograms of STM-BJ measurements at 40 and 100 min. According to previous measurements, the electrode displacements of **MPP** and **OMPP** are 0.38 and 0.14 nm, respectively. The histogram was fitted by the Gaussian function, and the peaks assigned to molecular features are marked with **MPP** (red) and **OMPP** (blue). The peak areas were integrated to determine the number of traces with the specific molecular feature. Thus, we could determine the area ratio of **OMPP** with 60.744% (= 11.20966/(11.20966+7.24419) × 100%). Then the proportions of **MPP** and **OMPP** versus the reaction time, respectively (right column, (c). The applied bias potential is 50 mV. The applied bias potential is (d) 20 mV, (e) 50 mV, (f) 70 mV, (g) 80 mV and (h) 100 mV. The summarized reaction kinetics of single-molecule junctions under different bias voltages. The results show that the reaction kinetics of the aromatization reaction can be tuned by the applied EEF. The reaction rate for the transformation from compound **MPP** to **OMPP** varies under different bias voltages according to the fitted results in the main text (Fig. 2b). For the reaction process, the **IOA** was largely in excess (100 mmol/L). The reaction will occur upon the two solutions being mixed, and the

reactant of **IOA** will make a successful collision with molecule **MPP**, even when the **MPP** is captured between two electrodes. Meanwhile, the Menshutkin reaction can be considered a pseudo-first-order reaction. Since the concentration of **IOA** can be considered a constant, the proportion evolution with the reaction time scale can be fitted exponentially. Therefore, to extract the intrinsic kinetic information, the calculated proportion data were fitted as shown in the main text. Since the reaction can be considered as a quasi-first order reaction, the reaction time has an exponential relationship of $P = P_0 (1-\exp(-kt))$ with the proportion of the product, where P is the proportion of the compound **OMPP**, P_0 is the initial proportion of compound **MPP**, and k is the reaction rate constant. The k was fitted as 2.08×10^{-2} min^{-1}.

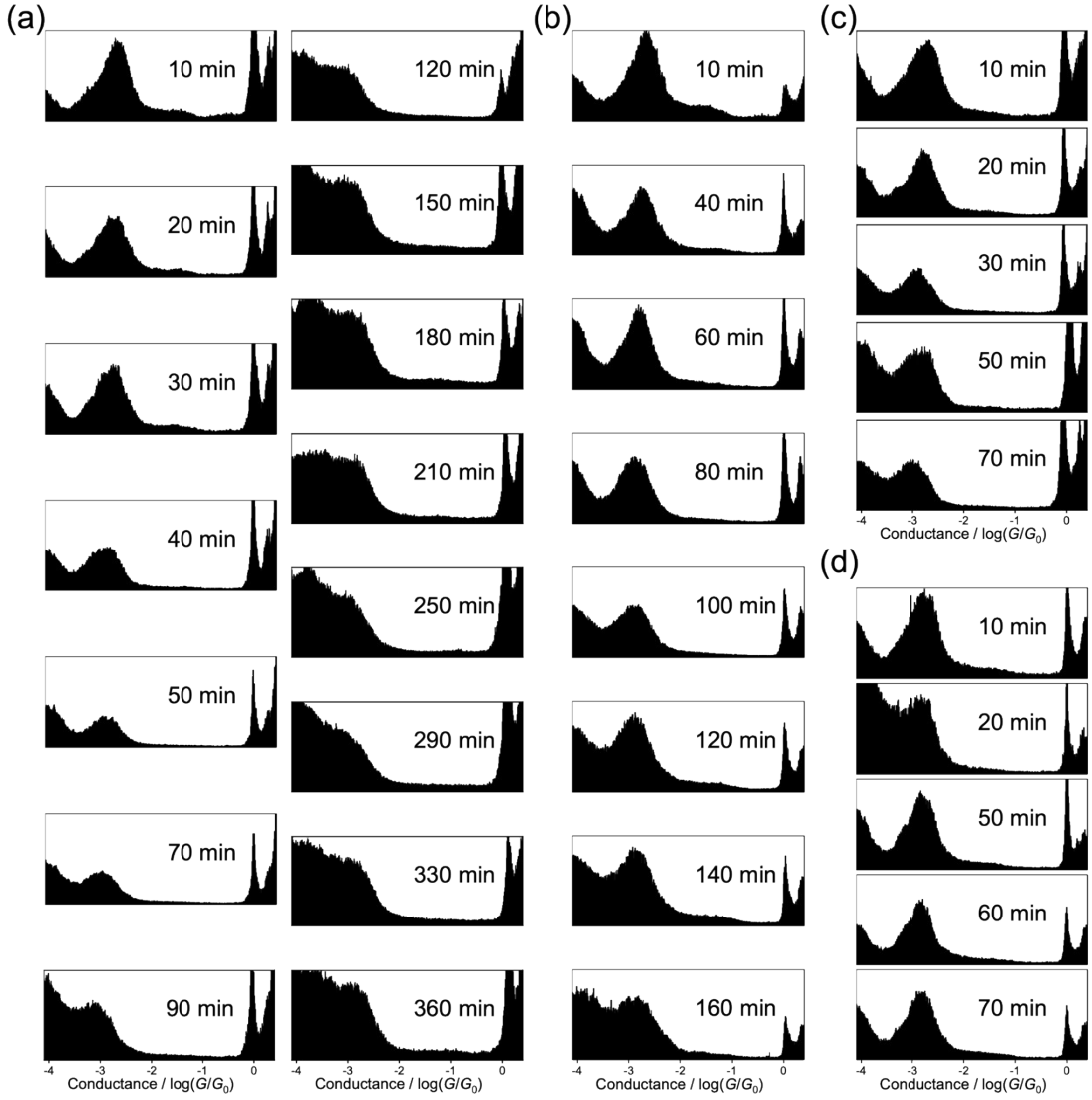

Fig. S16. 1D Conductance histograms as a function of time. (a-d) Reactions under a bias of 20, 70, 80 and 100 mV, respectively.

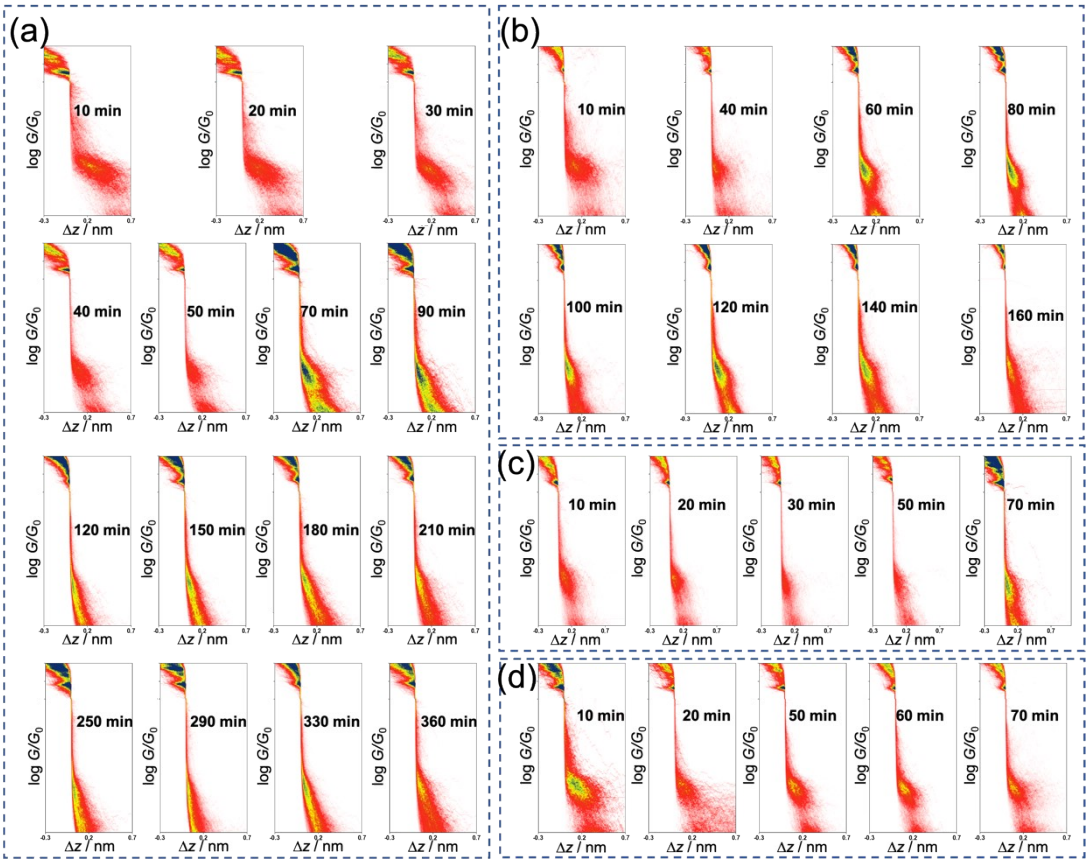

Fig. S17. 2D Conductance-distance histograms as a function of time. (a-d) Reactions under a bias of 20, 70, 80 and 100 mV, respectively.

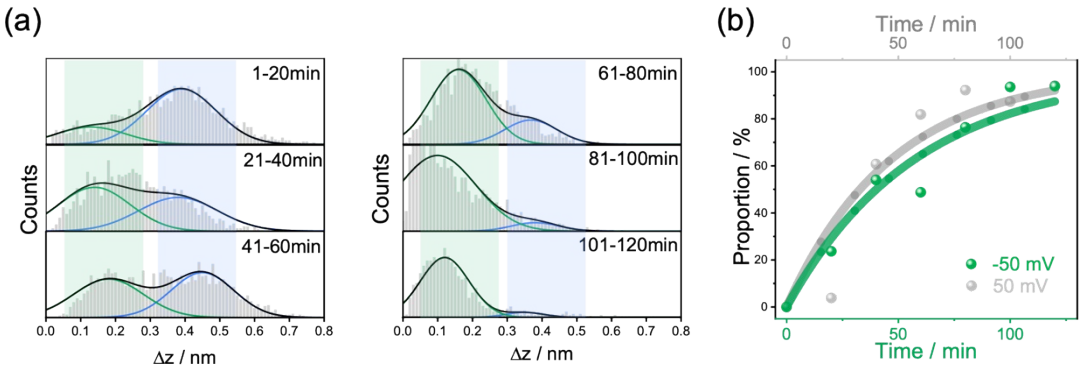

Fig. S18. Menshutkin reaction at a bias of -50 mV. (a) Length displacement histogram at -50 mV; (b) The proportion of **OMPP** extracted from 50 mV (grey dots) and -50 mV (green dots) as a function of time. The results show that the polarity of the bias voltage does not significantly affect the kinetics of the reaction, with a fitted reaction constant $k_{-50} = 1.73\times10^{-2}$ min^{-1}.

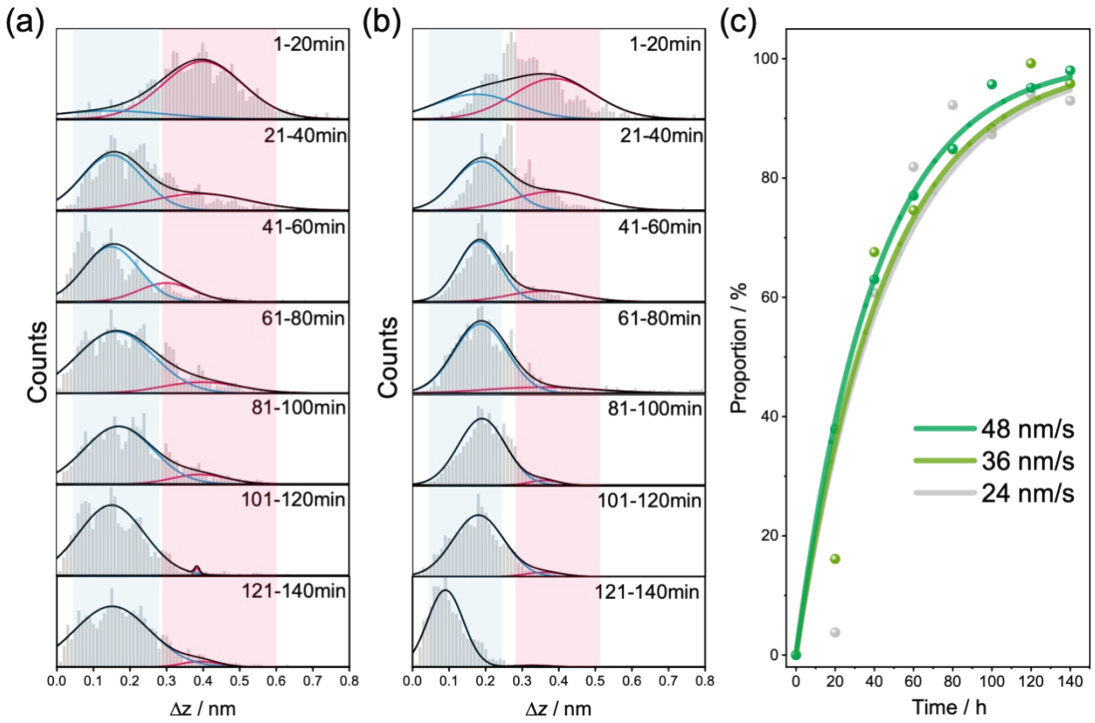

Fig. S19. Reaction rates determined from different piezo speeds of STM-BJ. Plateau distribution of the reaction by STM-BJ with a piezo speed of the (a) 36 nm/s and (b) 48 nm/s; (c) The proportion of **OMPP** extracted from the reaction where the piezo speed is 24 nm/s (the original value, grey), 36 nm/s (light green) and 48 nm/s (green), respectively. The fitted reaction rate constants are 2.08 10^{-2} min^{-1} at 24 nm/s, 2.20×10^{-2} min^{-1} at 36 nm/s and 2.49×10^{-2} min^{-1} at 48 nm/s.

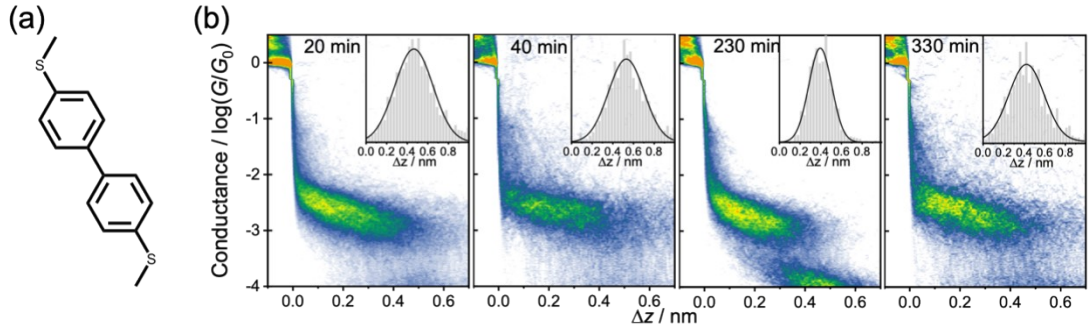

Fig. S20. STM-BJ measurement of the mixed solution of 1 mM BPY and 100 mM IOA. (a) The structure of 4,4'-bis(methylthio)-1,1'-biphenyl (**BPY**). (b) 2D histograms at 20, 40, 230 and 330 minutes, respectively. Insets: plateau length histograms. **BPY** could still be captured even after 5 hours (330 min), suggesting that **IOA** cannot compete with -SMe anchor for forming single-molecule junctions.

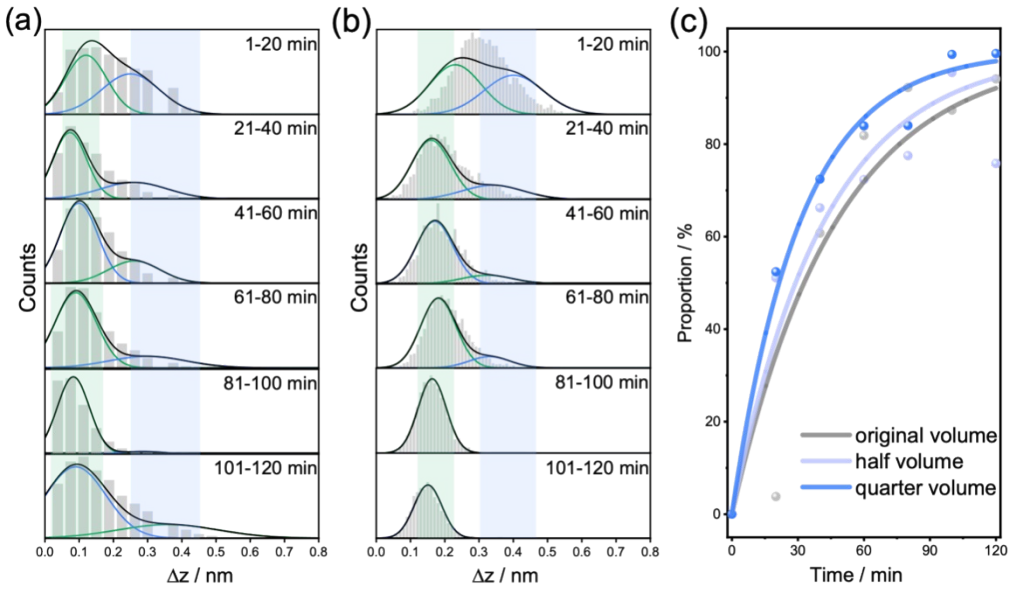

Fig. S21. Reaction volumes variation experiment. Plateau distributions of half (a) and quarter (b) volume of the Menshutkin reaction under a bias of 50 mV. (c) The proportion of **OMPP** extracted from the original (grey), half (light blue) and quarter (blue) volume of the reactions. As the volume of solution in the STM-BJ liquid cell decreases, the reaction rate slightly increases.

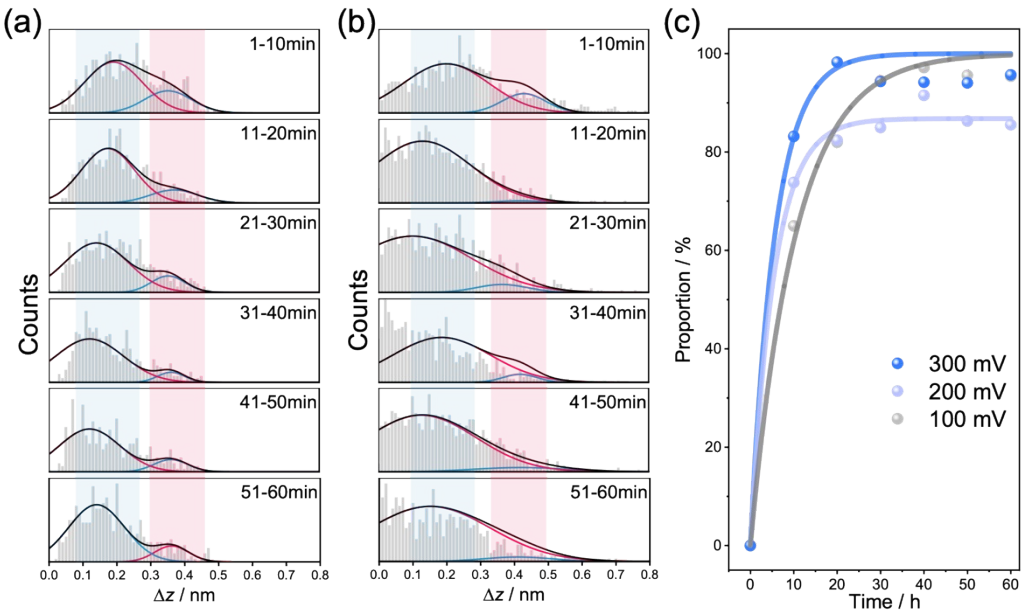

Fig. S22. Bias variation experiment. Plateau distributions of the (a) 200 mV and (b) 300 mV reaction. (c) The proportion of **OMPP** extracted from the 100 mV (grey), 200 mV (light blue) and 300 mV (blue) reactions. The derived reaction constants are k_{200} = 1.77×10^{-1} min^{-1} and k_{300} = 1.84×10^{-1} min^{-1}. As a higher bias would lead to instability of the experiment, the reaction rates are estimated values.

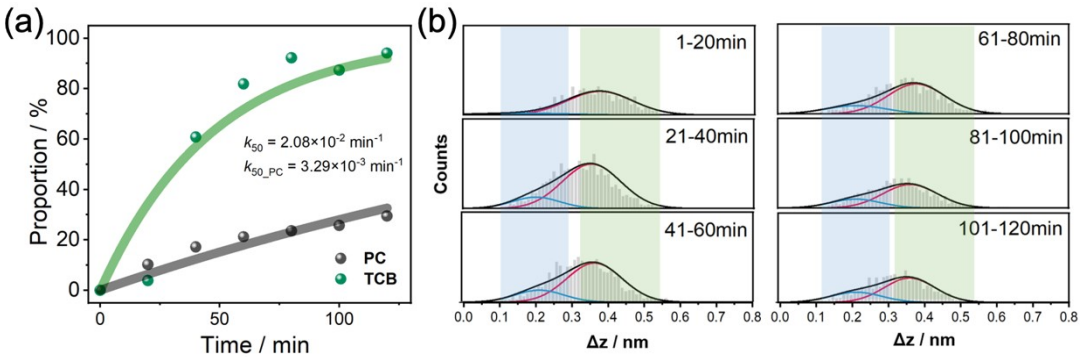

Fig. S23. Menshutkin reaction with polar solvents. (a) The proportion of **OMPP** extracted from the PC (black) and TCB (green) as solvents. (b) Plateau distributions of the Menshutkin reaction in PC.

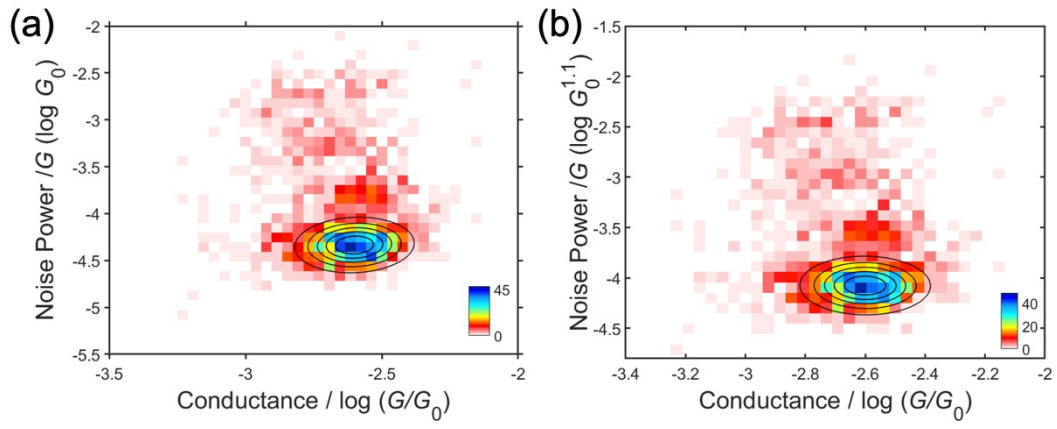

Fig. S24. Flicker noise measurement of MPP. The 2D histogram of flicker noise power density (a) and normalized by $G_0^{1.1}$. (b) versus the average conductance for MPP.

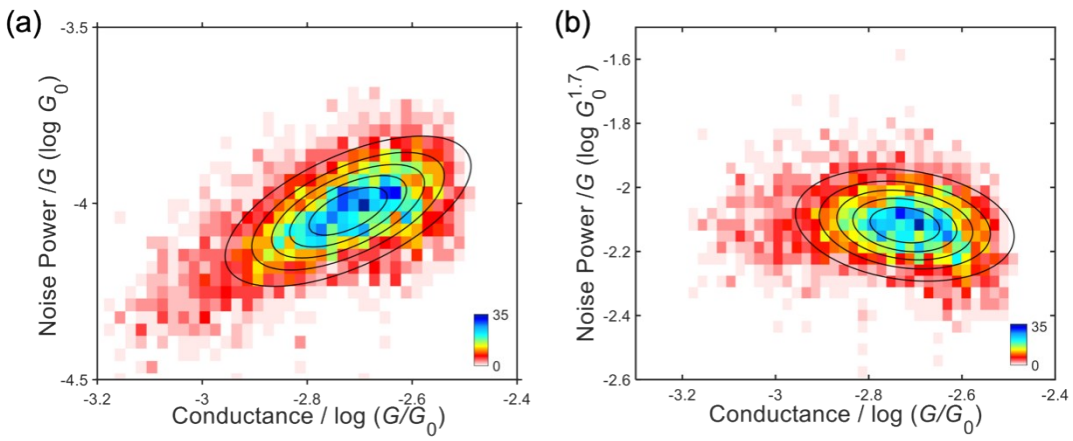

Fig. S25. Flicker noise measurement of OMPP. The 2D histogram of flicker noise power (a) and normalized by $G_0^{1.7}$. (b) versus the average conductance for **OMPP**.

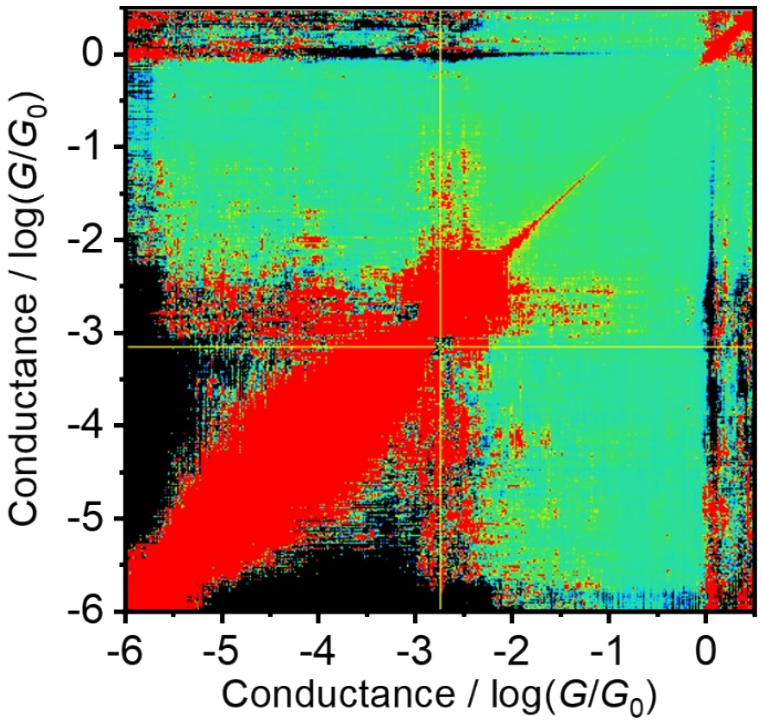

Fig. S26. The 2D covariance histograms of compiled data. It shows a clear non-correlation area (two yellow lines) between the **MPP** and **OMPP** values during the detection of the reaction by STM-BJ, which means that the two conductance plateaus occurred with no covariance.

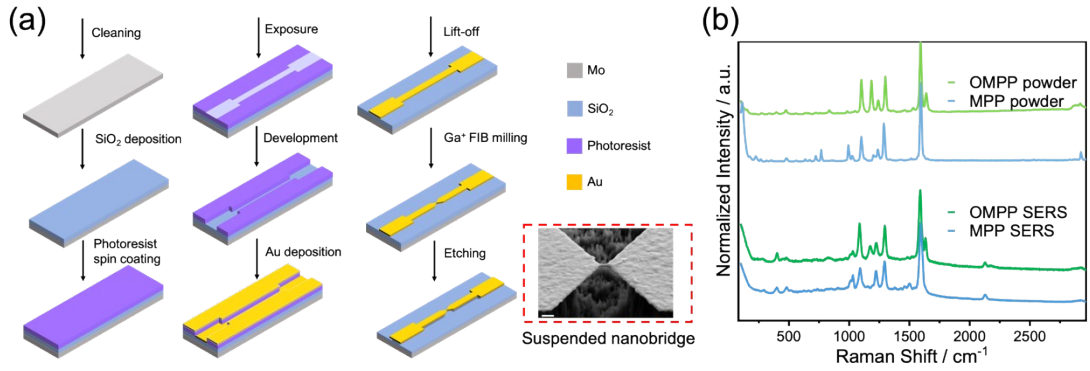

Fig. S27. The fabrication method of microchips for MCBJ. (a) The fabrication method of MCBJ chip. The scale bar in the inset equals 200 nm. (b) Raman spectra of **MPP** and **OMPP**. Powder: top; SERS: bottom.

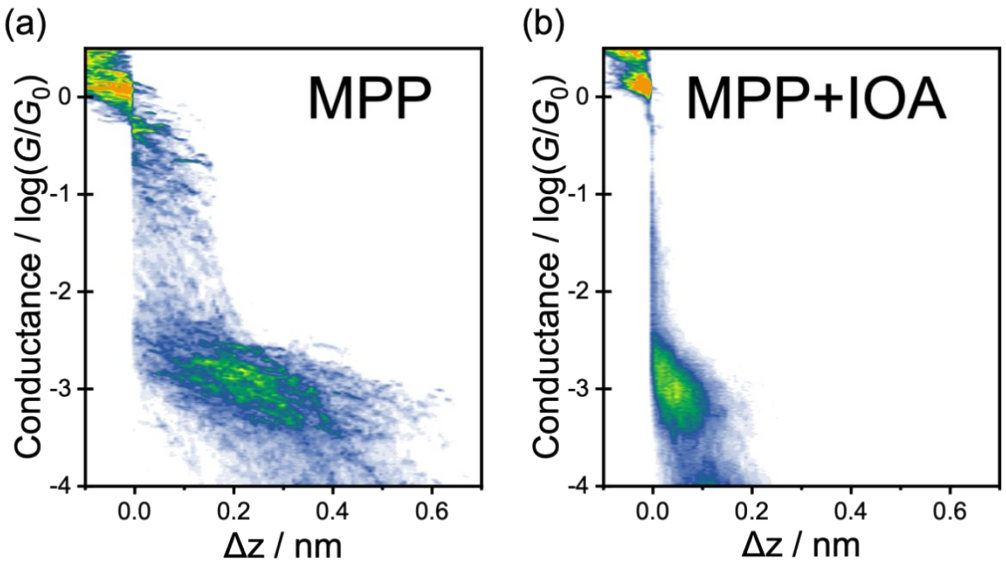

Fig. S28. 2D conductance-distance histogram of MCBJ measurements. (a) 1mM **MPP** constructed from 349 conductance-distance traces; (b) Mixed solution of 1 mM **MPP** and 100 mM **IOA** to give the Menshutkin reaction. The 2D histogram was constructed from 331 conductance-distance traces.

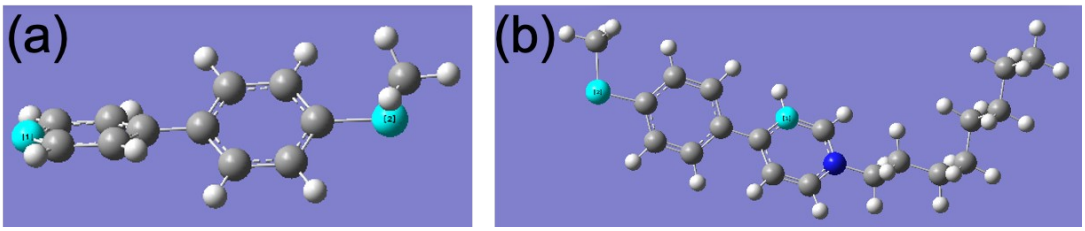

Fig. S29. Optimized molecular structures of MPP and OMPP. Lightened atoms show the possible anchoring sits, and the distance between two atoms is 0.89 nm for **MPP** (a) and 0.69 nm for **OMPP** (b), respectively.

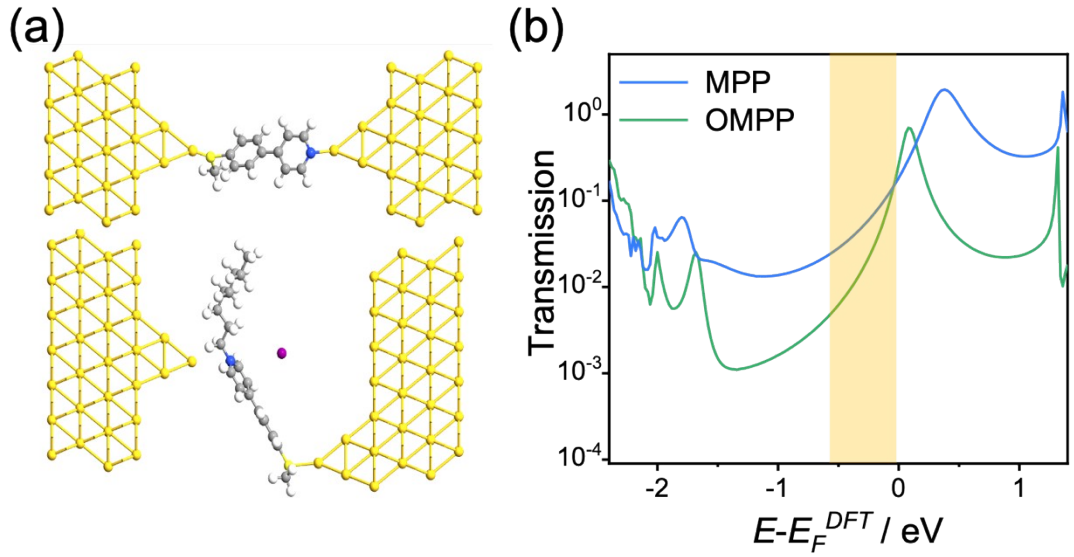

Fig. S30. The theoretical calculation carried out by DFT. (a) Optimized geometry of **MPP** (top) and **OMPP** (bottom) junctions. (b) The calculated transmission of **OMPP** and **MPP**.

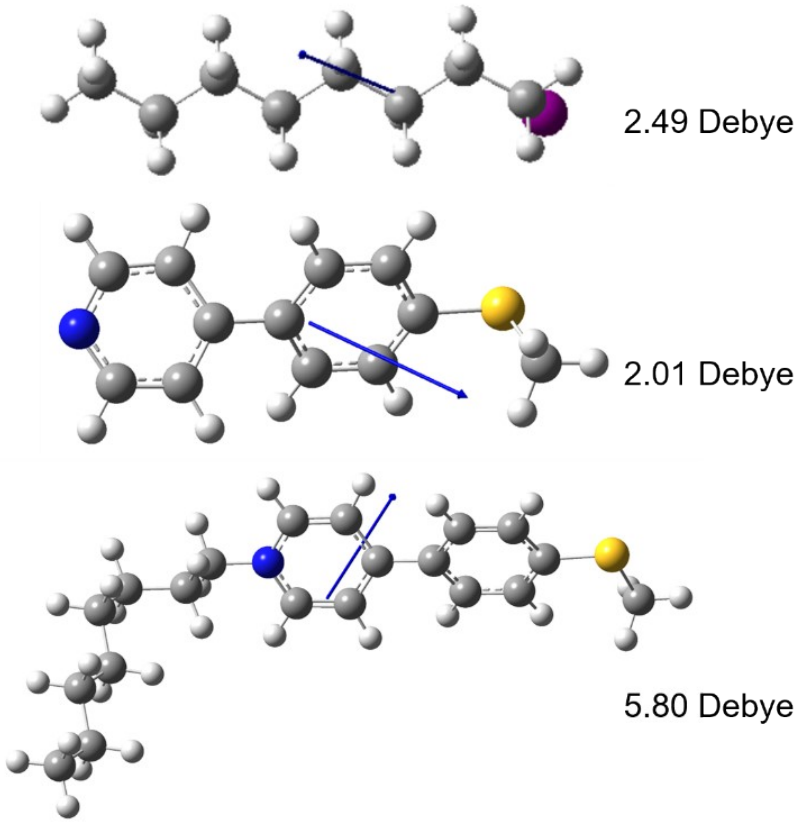

Fig. S31. Dipole moments of IOA, MPP and OMPP.

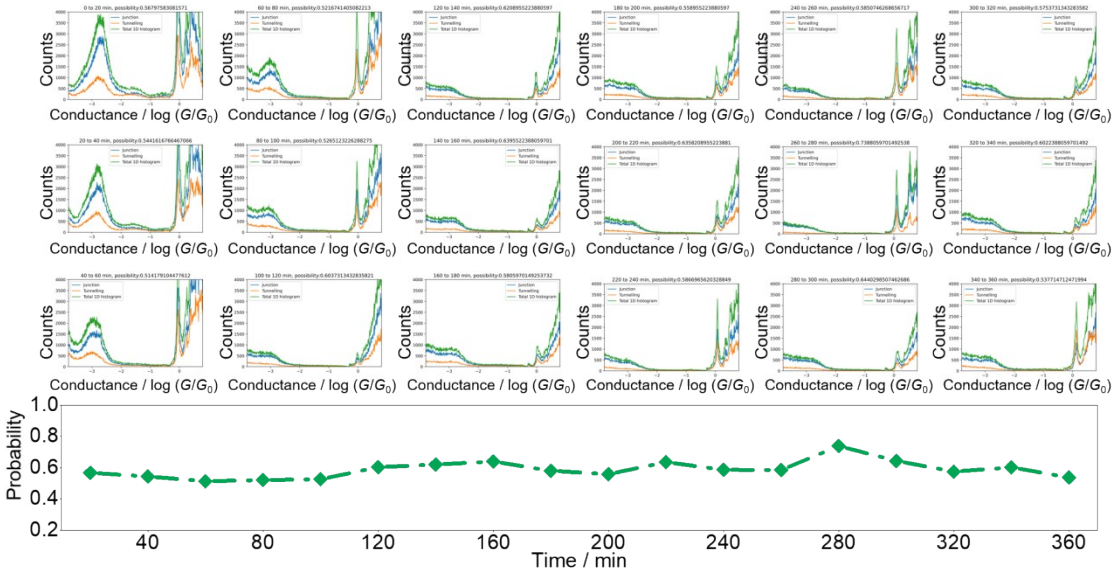

Fig. S32. Clustered 1D histograms and junction formation probabilities of different time intervals at 20 mV.

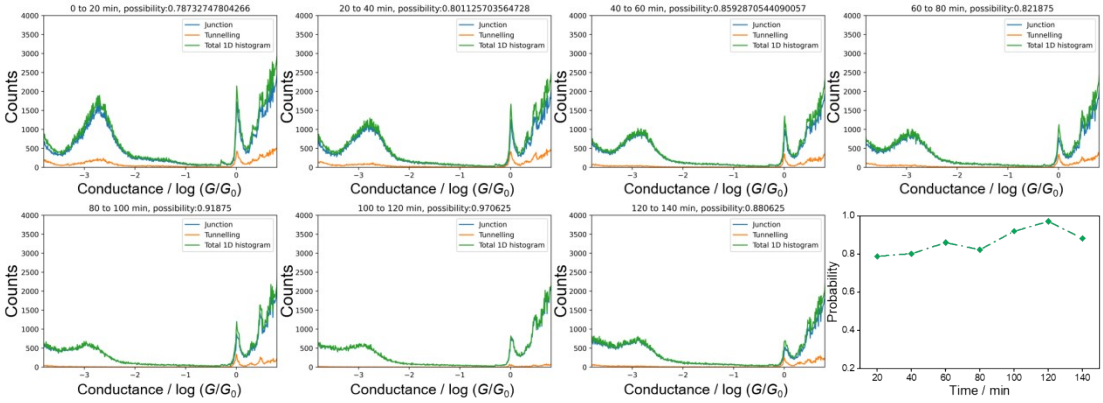

Fig. S33. Clustered 1D histograms and junction formation probabilities of different time intervals at 50 mV.

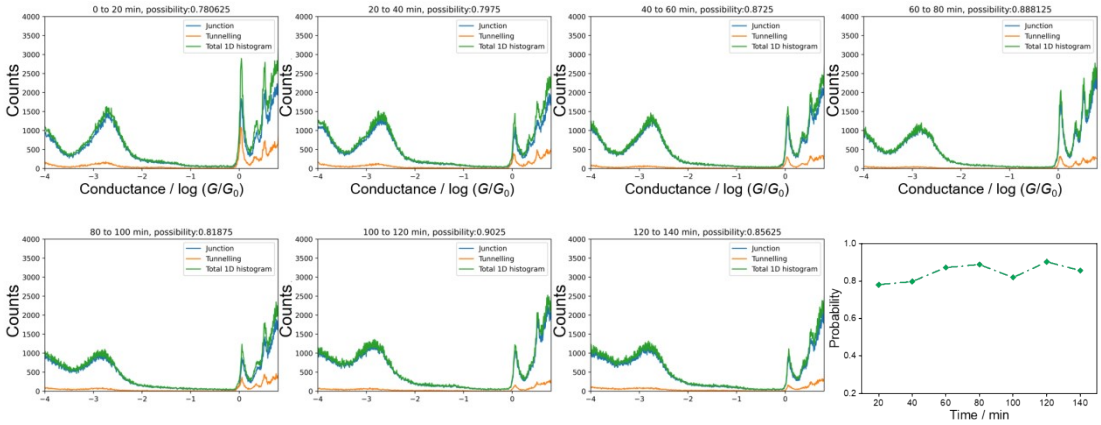

Fig. S34. Clustered 1D histograms and junction formation probabilities of different time intervals at 70 mV.

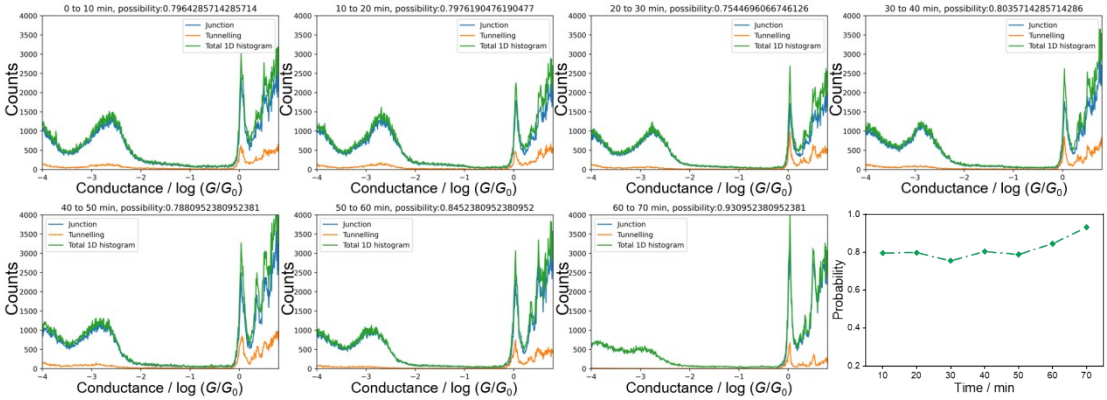

Fig. S35. Clustered 1D histograms and junction formation probabilities of different time intervals at 80 mV.

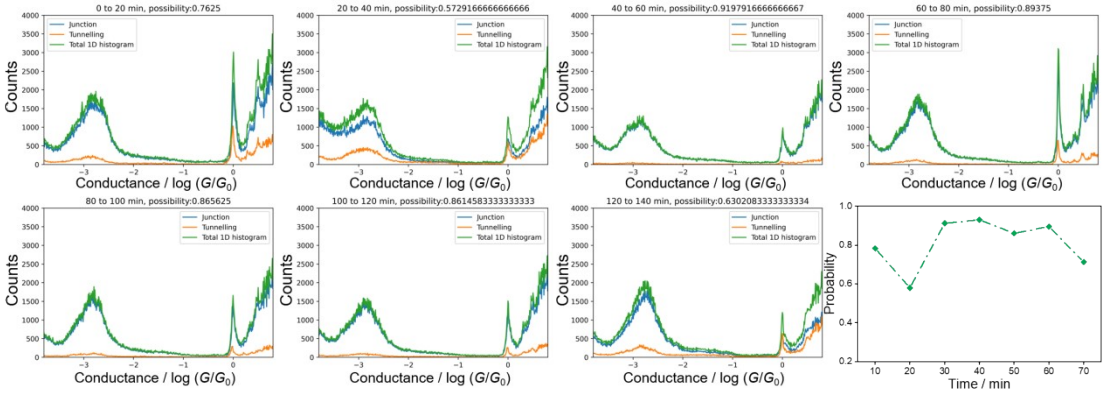

Fig. S36. Clustered 1D histograms and junction formation probabilities of different time intervals at 100 mV.

Entry	$k_{original}$		$k_{accelarated}$		Ratio	Reference
	Solvent	Reaction	Solvent	Reaction constant		
a	Cyclopentyl methyl	4.8×10^{2} $M^{-1}\cdot s$	DMSO	1.57×10^{2} $M^{-1}\cdot s$	3.27	*Green Chem.*,
b	Benzene	1*	Ethyl alcohol	6.3*	6.3	Z. Phys. Chem.,
c	Benzene	744 $M^{-1}\cdot s^{-1}$	Iodobenzene	5220 $M^{-1}\cdot s$	7.0	*J. Org. Chem.*,
d	Benzene	1*	Nitrobenzene	25.0*	25.0	J. Am. Chem.
e	Benzene	0.0239 M^{-}	o-$C_6H_4^-NO_2^-$Cl	1.10 $M^{-1}\cdot min^{-1}$	46.0	*Z. Phys. Chem.*,
f	TCB	2.46×10^{-6} min^{-1}	DMSO	1.45×10^{-4} min^{-1}	58.9	This work
g	Benzene	0.23×10^{-5} M^{-}	DMSO	31.74×10^{-5} M^{-}	138.0	*Chem. Eng. J.*,
h	Toluene	3.37 $M^{-1}\cdot s^{-1}$	DMSO	873.0 $M^{-1}\cdot s^{-1}$	259.1	J. Chem. Soc.
i	Toluene	1.61×10^{-6} M^{-}	Nitromethane	6.09×10^{-4} $M^{-1}\cdot s^{-}$	378	Nat. Chem.,
j	Butyl bromide	0.075 $M^{-1}\cdot s^{-1}$	Butyl bromide	120	1600	J. Am. Chem.
k	TCB	2.46×10^{-6} min^{-1}	TCB with EEF	9.60×10^{-2} min^{-1}	390000	This work

Table S1. Summary of different Menshutkin reaction systems accelerated by solvents.

Reference:

1. F. Ciesa, A. Plech, C. Mattioli, L. Pescatori, A. Arduini, A. Pochini, F. Rossi and A. Secchi, *J. Phys. Chem. C*, 2010, **114**, 13601-13607.
2. O. Adak, E. Rosenthal, J. Meisner, E. F. Andrade, A. N. Pasupathy, C. Nuckolls, M. S. Hybertsen and L. Venkataraman, *Nano Lett.*, 2015, **15**, 4143-4149.

3. S. He, R. Tian, W. Wu, W.-D. Li and D. Wang, *Int. J. Extrem. Manuf.*, 2021, **3**, 012001.
4. C. Zhan, G. Wang, X. G. Zhang, Z. H. Li, J. Y. Wei, Y. Si, Y. Yang, W. Hong and Z. Q. Tian, *Angew. Chem. Int. Ed.*, 2019, **58**, 14534-14538.
5. H. Wen, W. Li, J. Chen, G. He, L. Li, M. A. Olson, A. C.-H. Sue, J. F. Stoddart and X. Guo, *Sci. Adv.*, 2016, **2**, e1601113.
6. L. Xiang, J. L. Palma, Y. Li, V. Mujica, M. A. Ratner and N. Tao, *Nat. Commun.*, 2017, **8**, 14471.
7. C. Huang, M. Jevric, A. Borges, S. T. Olsen, J. M. Hamill, J. T. Zheng, Y. Yang, A. Rudnev, M. Baghernejad, P. Broekmann, A. U. Petersen, T. Wandlowski, K. V. Mikkelsen, G. C. Solomon, M. Brondsted Nielsen and W. Hong, *Nat. Commun.*, 2017, **8**, 15436.
8. W. Hong, H. Valkenier, G. Mészáros, D. Z. Manrique, A. Mishchenko, A. Putz, P. M. García, C. J. Lambert, J. C. Hummelen and T. Wandlowski, *Beilstein J. Nanotech.*, 2011, **2**, 699-713.